Acta Oceanol. Sin., 2023, Vol. 42, No. 2, P. 150–162
https://doi.org/10.1007/s13131-022-2063-8
http://www.aosocean.com
E-mail: ocean2@hyxb.org.cn

Shallow sea topography detection using fully polarimetric Gaofen-3 SAR data based on swell patterns

Longyu Huang[1], Chenqing Fan[1, 2], Junmin Meng[1, 2*], Jungang Yang[1, 2], Jie Zhang[1, 2]

[1] Laboratory of Marine Physics and Remote Sensing, First Institute of Oceanography, Ministry of Natural Resources, Qingdao 266061, China

[2] Ocean Telemetry Technology Innovation Center, Ministry of Natural Resources, Qingdao 266061, China

Received 12 November 2021; accepted 9 May 2022

© Chinese Society for Oceanography and Springer-Verlag GmbH Germany, part of Springer Nature 2023

Abstract

Compared to single-polarization synthetic aperture radar (SAR) data, fully polarimetric SAR data can provide more detailed information of the sea surface, which is important for applications such as shallow sea topography detection. The Gaofen-3 satellite provides abundant polarimetric SAR data for ocean research. In this paper, a shallow sea topography detection method was proposed based on fully polarimetric Gaofen-3 SAR data. This method considers swell patterns and only requires SAR data and little prior knowledge of the water depth to detect shallow sea topography. Wave tracking was performed based on preprocessed fully polarimetric SAR data, and the water depth was then calculated considering the wave parameters and the linear dispersion relationships. In this paper, four study areas were selected for experiments, and the experimental results indicated that the polarimetric scattering parameter α had higher detection accuracy than quad-polarization images. The mean relative errors were 14.52%, 10.30%, 12.56%, and 12.90%, respectively, in the four study areas. In addition, this paper also analyzed the detection ability of this model for different topographies, and the experiments revealed that the topography could be well recognized when the topography gradient is small, the topography gradient direction is close to the wave propagation direction, and the isobath line is regular.

Key words: fully polarimetric SAR, shallow sea topography, Gaofen-3, swell patterns

Citation: Huang Longyu, Fan Chenqing, Meng Junmin, Yang Jungang, Zhang Jie. 2023. Shallow sea topography detection using fully polarimetric Gaofen-3 SAR data based on swell patterns. Acta Oceanologica Sinica, 42(2): 150–162, doi: 10.1007/s13131-022-2063-8

1 Introduction

The shallow sea near the coast is the main area of human marine activities. Measurement of shallow sea topography provides not only an important guarantee for shallow water resource development, coastal engineering construction, navigation safety, marine rescue, etc., but also an important guarantee for dynamic monitoring and management of the military marine environment, and evaluation of the offshore economy and environment. The traditional topography detection method involves on-site surveys via ships, such as sonar or multibeam echosounders, which suffer notable limitations. For example, this method can only obtain the water depth in a small area, which is a time-consuming and laborious process with a low economic efficiency, and this method cannot cover disputed sea areas. With the continuous development of remote sensing technology, the adoption of synthetic aperture radar (SAR) to detect shallow sea topography has become a research area of heightened interest in recent years. SAR can observe the sea surface throughout the day, with a high spatial resolution, large coverage, low-cost and high time efficiency, which provides a new method for underwater topography detection in shallow sea areas.

There are two main methods to detect shallow sea topography based on SAR data. The first method considers the interaction between strong currents and the local seabed topography, which leads to changes in sea surface roughness (Alpers and Hennings, 1984). This method depends on the interaction between waves and currents to generate visible radar signals under favorable tidal and wind conditions (Huang et al., 2021) and is effective for sand ridge bottom topography (Li et al., 2009). Additionally, SAR could also image topography even under deep water (500 m underwater) as long as the tide is strong enough (Li et al., 2010b; Zheng et al., 2012), but this method is strongly dependent on the initial water depth, and the resolution of the detected topography is coarse.

The second type of topography inversion technique relies on the refraction and shallow water effects of long-surface gravity waves propagating toward the coast and can establish a direct relationship between swells and the water depth. This approach mainly includes the calculation of wave parameters and the water depth with linear dispersion relationships. It applies to simple wave systems. There are three necessary conditions: (1) the water depth should less than the half wavelength, (2) existing obvious swell patterns in the SAR image, and (3) assuming the same wave train (Bian et al., 2016).

Wave features are presented as textures on SAR images, and frequency domain analysis is one of the main methods used to study textures. Currently, wave extraction methods based on the fast Fourier transform (FFT) and wavelet transform have been developed (Brusch et al., 2011; Santos et al., 2020). Pereira et al. (2019) study showed that the FFT had favorable stability in calculating the wavelength and wave direction of SAR images. The FFT extracts the dominant wavelength in a certain region, and the

Foundation item: The National Natural Science Foundation of China under contract Nos 51839002 and U2006207.
*Corresponding author, E-mail: mengjm@fio.org.cn

wavelength can be obtained more precisely when the sub-image size is set to 4–8 times the wavelength (Shen et al., 2019). The method requires significant swell features on the SAR image. The wavelength will be too large (the scale can reach kilometers) when there exists a mass of speckle noise, and the wave tracking can be enhanced by setting the filter and limiting the range of wavelength and wave direction (Boccia et al., 2014, 2015a).

The linear dispersion relationship describes the quantitative relationship between wave and water depth, which has different sensitivities to input parameters (wavelength, wave period, and initial water depth), where wave period has the greatest effect on water depth and initial water depth has the least (Bian et al., 2020; Boccia et al., 2015b). The interaction between waves and the bottom topography only occurs in shallow water areas. However, this method has difficulty retrieving extreme shallow water depths. To address this problem, Pleskachevsky and Ankita Misra (Misra et al., 2022; Pleskachevsky et al., 2011) proposed an approach to detect shallow topography using SAR and optical remote sensing images and acquired water depths in extremely shallow regions.

The shallow sea topography detection technology based on the linear dispersion relationship has been developed many years, and multiple SAR satellite (ERS-2, RESAT-1, Sentinel-1 and HJ-1C) data have been validated (Bian et al., 2016, 2018; Fan et al., 2008; Mishra et al., 2014; Santos et al., 2022). However, the above studies mainly used single-polarization SAR data. To explore the capability of fully polarimetric SAR data in shallow sea topography detection, this paper proposes a new approach based on the polarization scattering parameter α because the parameter performs well in wave measurements (Schuler et al., 2004, 2005). Finally, Gaofen-3 fully polarimetric SAR data were adopted for validation, and the feasibility of fully polarimetric SAR data in shallow sea topography detection was preliminarily examined.

This paper is structured as follows: Section 2 describes the SAR data and other auxiliary data pertaining to the study area and the theoretical basis; Section 3 outlines the experimental procedure of underwater topography detection in the sea off Xiapu County, Fujian Province, China and the results of topography detection in the four study areas; Section 4 analyses the detection capabilities of the different parameters and the responsiveness of this model to different terrains; and finally, Section 5 provides the conclusions.

2 Materials and methods

2.1 *Study areas and data*

In this paper, four study areas were selected for testing, namely, the eastern offshore area of Hoi An, Vietnam; the southern offshore area of Pingtan County, Fujian Province, China; the eastern offshore area of Xiapu County, Fujian Province, China; and the western offshore area of Rakhine State, Myanmar, denoted as study areas A, B, C and D, respectively. These four study areas exhibit slight topographic variations, shallow water depths and strong swell characteristics, which are suitable for the detection of offshore topography. The locations of the areas are shown in Fig. 1.

2.1.1 *SAR data*

In this paper, we adopted four scenes of fully polarimetric Gaofen-3 SAR data, and the specific information is provided in Table 1. The Gaofen-3 satellite is the first SAR satellite in China's Gaofen special program, which was launched in August 2016 and carries a C-band multi-polarization synthetic aperture radar with a spatial resolution of 1–500 m and swaths ranging from 10–650 km, which can not only realize global large-scale resource and environmental surveys, but can also realize fine identification of land and sea targets. The Gaofen-3 satellite is equipped with 12 imaging modes, including the traditional strip imaging mode and scanning imaging mode, in addition to the wave and global observation imaging modes applied in ocean analysis, which is the world's largest on-board SAR instrument with the most imaging modes thus far.

2.1.2 *Reference topography data*

Reference bathymetry data originating from two sources were considered in this paper, namely, SRTM15+ bathymetry data pertaining to study areas A, B and D, whereas the global General Bathymetric Chart of the Oceans (GEBCO) data pertaining to area C because SRTM15+ depth data are not available in study area C. SRTM15+ provides global bathymetric and topographic gridded data using a spatial resolution of 15 arc seconds, with bathymetric data combining ship measurements and satellite soundings (Tozer et al., 2019). The GEBCO is a continuous global model of ocean and land topography with a spatial resolution of 15 arc seconds, which is primarily based on multibeam survey data and provides global topographic data in a gridded form (Weatherall et al., 2021). GEBCO was generated by adding a large amount of measured data to SRTM15+ gridded data, both of which exhibit the same spatial resolution, so the GEBCO data were used as the alternative for SRTM15+ data.

2.2 *Topography detection principle of shallow sea*

In this paper, we applied the shallow sea topography detection model based on swell patterns and linear dispersion relationships. This model mainly included SAR wave imaging, wave shoaling and refraction theory and linear dispersion relationships. To explore the application of fully polarimetric SAR data in shallow sea topography detection, this paper selected $H/A/\bar{\alpha}$ decomposition techniques to process fully polarimetric SAR data and obtained the polarimetric scattering parameter α. The basic theory of the shallow sea topography detection model is introduced below.

2.2.1 *Wave imaging of SAR*

SAR can transmit electromagnetic signals and receive backscattered signals; the intensity of backscattered signals is determined by the roughness of the sea surface. Therefore, SAR images can indirectly represent the changes in sea surface roughness caused by waves. When small-scale waves on the sea surface satisfy the Bragg condition, they are referred to Bragg waves (Hasselmann et al., 1985),

$$\lambda_{\mathrm{Bragg}} = \frac{\lambda_{\mathrm{SAR}} \sin\theta}{2}, \tag{1}$$

where λ_{Bragg} and λ_{SAR} are the wavelengths of the Bragg waves and the radar incident waves, respectively. θ is the local incidence angle. Bragg scattering is the main sea surface backscattering mechanism when the incidence angle of the radar wave is 20°–60°.

Short Bragg waves are modulated by long oceanic gravity waves. The process of SAR imaging of long ocean waves can be described based on Bragg scattering and the two-scale approximation (Hasselmann et al., 1985). The model comprises three modulation mechanisms: tilt modulation, hydrodynamic modulation, and velocity bunching modulation. Tilt modulation suggests that the slope of the gravity wave changes the local incid-

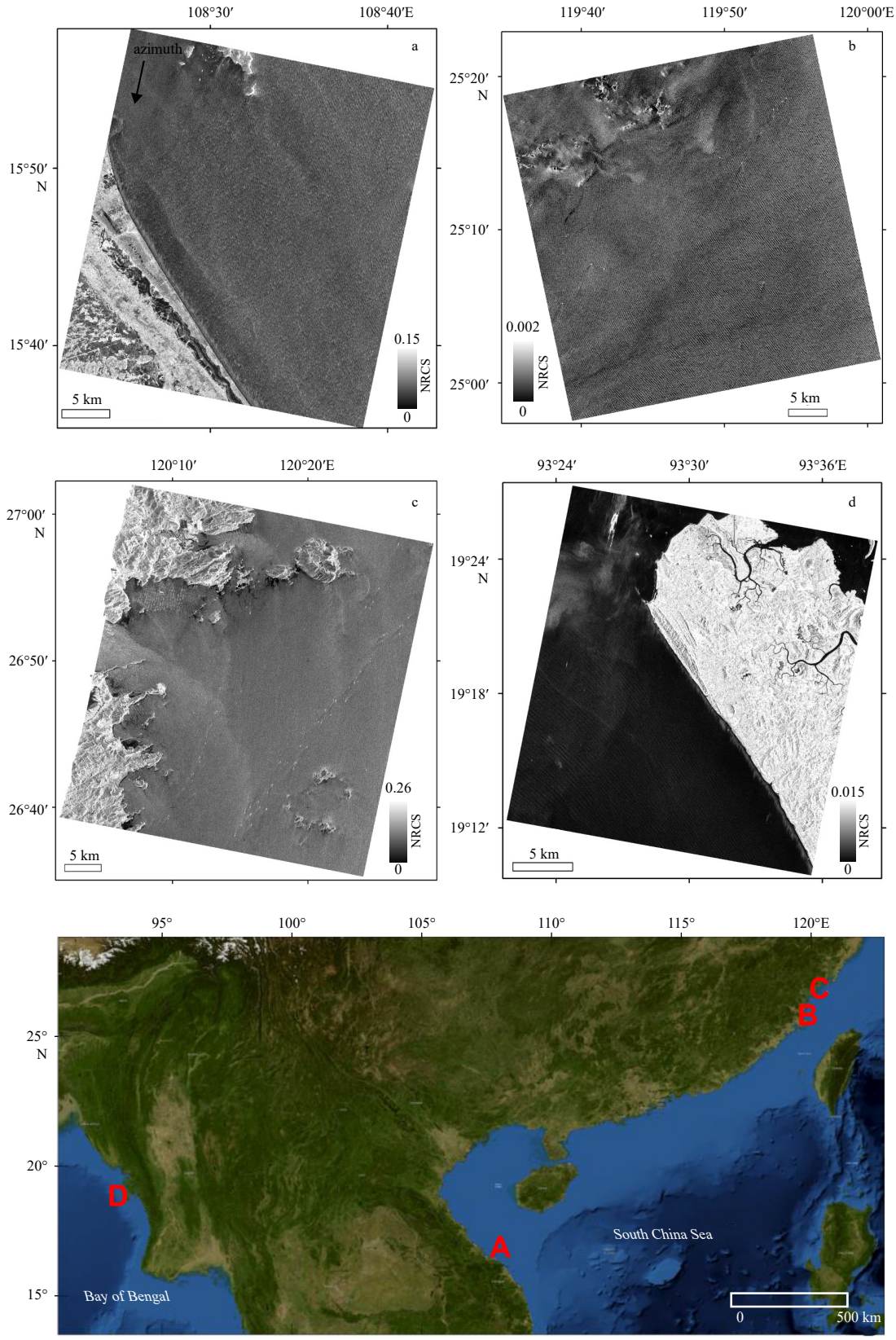

Fig. 1. Schematic diagram of the study area. The red letters in the map indicate the locations of the four study areas. a–d. HH-polarized images of SAR intensity data that we collected for four study areas (A–D).

ence angle and therefore the Bragg wavelength and backscatter intensity. Hydrodynamic modulation is caused by the orbital motion of water particles within the gravity wave. This leads to convergence of capillary waves at the wave crest and divergence of capillary waves in the oceanic gravity wave trough. As a result, the crests of the long waves appear brighter in the SAR images.

Table 1. Gaofen-3 satellite parameters and SAR image information

Study area	Image ID	Imaging time	Pixel resolution	Range of incidence
A	I-1	2018-12-30 22:42	8 m	31.07°–33.09°
B	I-2	2020-09-02 10:01	8 m	23.91°–26.57°
C	I-3	2020-09-24 22:06	8 m	25.66°–28.28°
D	I-4	2020-09-17 23:37	8 m	43.21°–44.44°

Velocity bunching modulation indicates that the motion of long waves alters the imaging process specific to SAR imaging systems. If the azimuthal displacement is smaller than one wavelength, waves along the azimuthal direction can be linearly represented in the SAR image. In contrast, when the displacement is larger than a certain wavelength, wave mapping via SAR images can be nonlinear and distorted. Tilt modulation and hydrodynamic modulation impose the greatest effect on SAR echoes when long waves propagate along a direction perpendicular to the motion direction of the SAR platform.

SAR cannot image azimuthal traveling waves shorter than a certain threshold. This threshold is the SAR azimuthal cut-off wavelength. The cut-off wavelength $A_{\min}$ can be expressed with the following empirical relationship (Beal et al., 1983),

$$A_{\min} = \frac{R}{V_{\mathrm{SAR}}}\sqrt{H_{\mathrm{s}}}, \tag{2}$$

where V_{SAR} is the velocity of the satellite platform, R is the slant range and H_{s} is the significant wave height.

2.2.2 *Wave shoaling and refraction*

If the water depth is less than half the wavelength, the wave is in shallow water, at which point the surface wave perceives the bottom topography and is in turn shoaled and refracted. If a long sea wave propagates into shallow water, the wave is decelerated. This results in wavelength shortening. The wave height increases due to energy conservation. These two effects increase the steepness of the wave. The deceleration process coupled with the abovementioned increases in the wave height and steepness is referred to as the wave shoaling theory. If the crest of a wave is not aligned with the contour line of the bottom topography, wave refraction occurs at a certain angle between the wave direction and the contour line. For example, part of the wave near the beach propagates in shallow water and slows down more than part away from the beach. Then part of the wave in shallow water is covered by the wave in deeper water, which causes a change in the direction of wave propagation and continues until the wave crest becomes parallel to the depth contours or the wave breaks.

2.2.3 *Linear dispersion relationships*

When wave occur in shallow water, the relationship between the water depth and waves can be described with the linear dispersion relationship (Calkoen et al., 2001; Kirby and Dalrymple, 1986),

$$\omega^2 = gk\tanh(kd), \tag{3}$$

where ω is the angular frequency of the wave ($\omega = \frac{2\pi}{T}$, and T is the wave period), g is the acceleration of gravity (9.8 m/s^2), k is the wavenumber ($k = \frac{2\pi}{L}$, and L is the wavelength) and d is the water depth. Transforming Eq. (3) yields the following relationship between the wavelength, water depth and angular frequency,

$$L = \frac{2\pi g}{\omega^2}\tanh\left(\frac{2\pi d}{L}\right). \tag{4}$$

2.2.4 *Retrieval of wave fields*

When a surface wave is visualized as a stripe in an SAR image, its wavelength can be calculated with the FFT. The FFT method decomposes a function in the spatial domain into its constituent frequency components. The FFT method is useful to obtain regular periodicity in an image. With the application of the FFT method, the sub-image can be converted into a 2D spectrum. The peaks in the 2D spectrum mark the wavelength and wave direction of all visible waves in the sub-image. The wavelengths and directions can be estimated with the following equations (Bruck and Lehner, 2013; Collard et al., 2005; Li et al., 2010a).

$$L = \frac{2\pi}{\sqrt{k_x^2 + k_y^2}}, \tag{5}$$

$$\phi = \arctan\left(\frac{k_y}{k_x}\right), \tag{6}$$

where L and ϕ are the sub-image peak wavelength and wave direction, respectively, and k_x and k_y are the coordinates of the peak in the two-dimensional wavenumber spectrum. Due to the static nature of SAR images, the acquired wave directions exhibit an ambiguity of 180°. Generally, information on the wave direction retrieved from the mutual spectrum or other sources must be considered to resolve this ambiguity. In coastal areas where wave undercurrents and refraction occur, the ambiguity can be resolved via manual inspection (Brusch et al., 2011).

2.2.5 *Polarimetric scattering parameter α*

As already described in Section 2.2.4, the wavelength can be determined from the peak coordinates in the wave spectrum, therefore the 2D wave spectrum is also crucial for shallow sea topography detection. Schuler et al. (2004, 2005) indicated that the polarimetric scattering parameter α was effective in retrieving the 2D wave spectrum and calculating other wave parameters (dominant wavelength, wave direction, wave height and wave period, etc.).

α is retrieved by the $H/A/\bar{\alpha}$ polarization decomposition technique (Appendix A) and is the key parameter for identifying the dominant scattering mechanism. The α parameter has desirable directional measurement properties, (1) it is roll-invariant in the azimuth direction and, (2) in the range direction, it is highly sensitive to wave-induced modulations of the local incidence angle. Thus, the α is well suited to make measurements of wave components traveling in the range direction. Wave spectra can be measured using the α parameter. Figure 1 shows that the waves propagated approximately along the range direction in the four study areas, so we adopted the α parameter to detect shallow sea topography.

2.3 *Accuracy evaluation indexes*

In this paper, two indexes were applied to evaluate the accuracy of the topography detection results, namely the mean absolute error (MAE) and the mean relative error (MRE).

$$\mathrm{MAE} = \frac{\sum_{i=1}^{n} |h_i - r_i|}{n}, \tag{7}$$

$$\mathrm{MRE} = \frac{\sum_{i=1}^{n} \left| \frac{h_i - r_i}{h_i} \right|}{n}, \tag{8}$$

where h_i and r_i are the detection and reference depths, respectively.

3 Results

Shallow sea topography detection is divided into four main processes: SAR preprocessing, wave tracking, water depth calculation and topography synthesis. The experimental flow chart is shown in Fig. 2.

3.1 *Polarimetric parameter extraction*

SAR pre-processing was divided into complex data conversion and polarimetric parameter extraction, and both processes were carried out in PIE-SAR 6.0 software. Complex data conversion entailed the conversion of raw SAR complex data into amplitude data (HH, HV, VV and VH polarized) through multi-looking processing, refined Lee filtering and geocoding. Polarimetric parameter was extracted as follows: first, the polarization matrix was converted from the original Gaofen-3 SAR data. Second, the refined Lee filter was applied to the polarization scattering matrix with a 5×5 filter window. Then, $H/A/\bar{\alpha}$ decomposition was applied to extract the polarimetric parameter α. Finally, these images were geocoded, and Fig. 3 shows the study area C result after pre-processing.

Wave features appear as texture distributions on SAR images, so we can analyze the presentation ability of waves in different SAR satellite imagery by evaluating the texture features (Zhao et al., 2013). In this paper, Tamura texture feature parameters (Appendix B) coarseness and contrast were adopted to analyze different SAR imagery. The analysis area is the red box in Fig. 3, with a size of 1 024×1 024 pixels. Table 2 shows the results that α has the largest coarseness and contrast. To some extent, α have a better performance than other polarimetric imagery in wave representation.

3.2 *Wave tracking*

The process of wave tracking is as follows:

(1) Wavelength threshold and wave period calculation

SAR cut-off wavelength depends on the orbital parameters of the satellite and sea state at the imaging time. In terms of image I-3 adopted in this paper, the satellite operating altitude is 755 km, the incidence angle at the imaging time is 23.44°, the slant range R can be calculated as 823 km, and the satellite operating velocity V_{SAR} is 7.47×10^3 m/s. Considering "Global Ocean Along-Track L3 Sea Surface Heights NRT" data, which can be downloaded from the corresponding website (https://marine.copernicus.eu/), the significant wave height at the imaging moment is determined as H_s=0.5 m, and finally by substituting the parameters into Eq. (2) to determine the cut-off wavelength A_{min}=78 m, the minimum wavelength detectable by the satellite reaches 78 m in this region.

In this section, four sub-images were selected for wave period estimation, and the sub-image size was set to 256×256 pixels. The

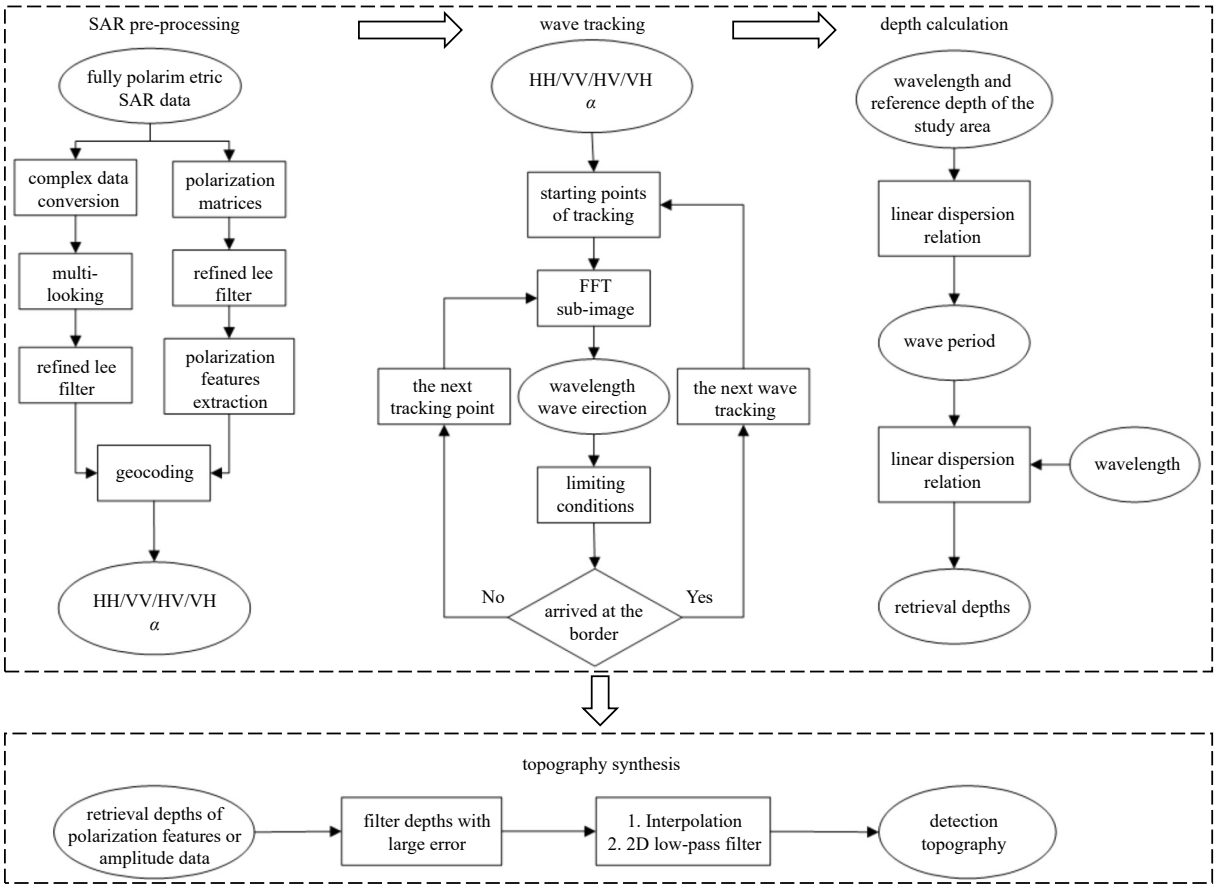

Fig. 2. Flow chart for shallow sea topography experiments.

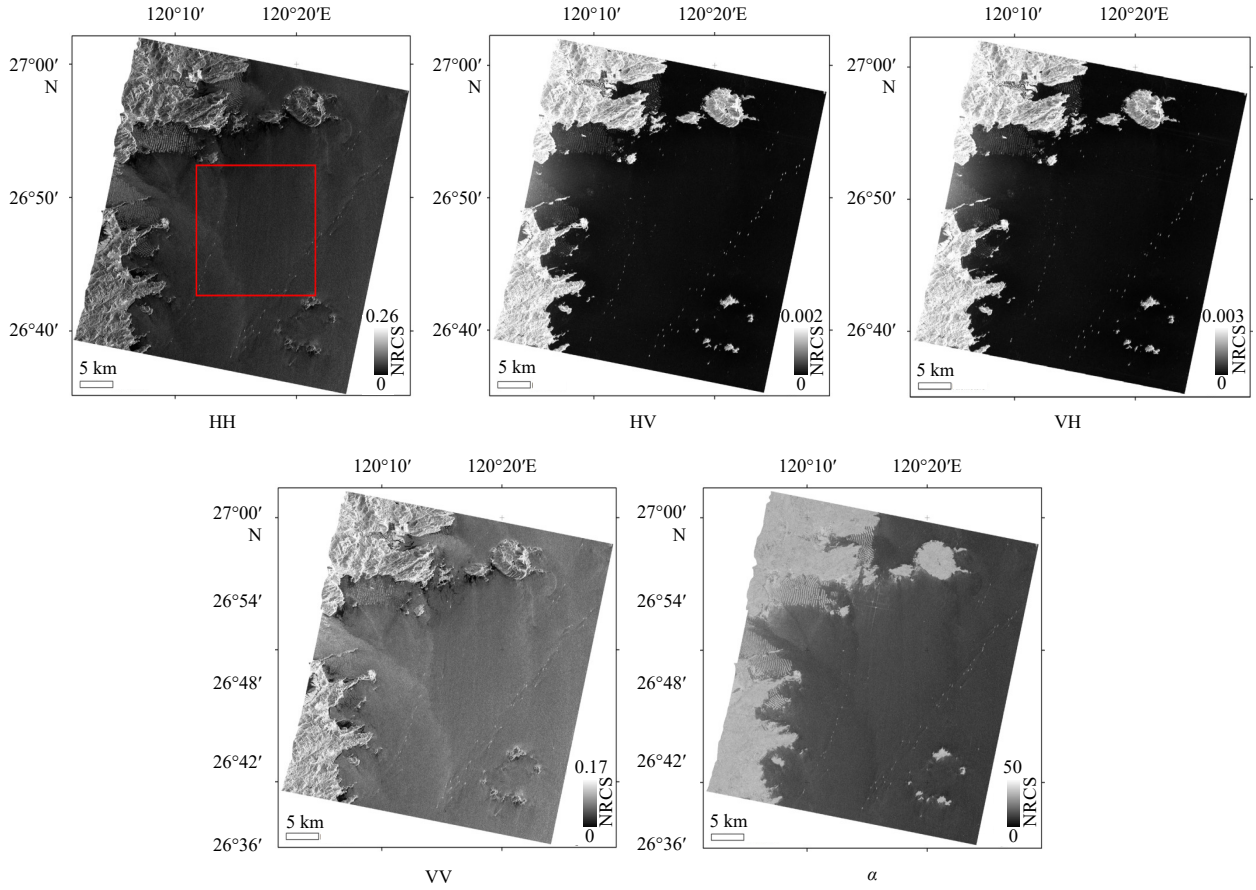

Fig. 3. The pre-processed intensity images and polarimetric parameter α (the unit is (°)) of SAR data in study area C.

Table 2. Texture analysis results of different parameters

Parameters	HH	VV	HV	VH	α
Contrast	13.87	13.76	13.67	13.67	15.34
Coarseness	0.008 1	0.008 1	0.000 5	0.000 5	1.526 0

wavelength could be obtained via spectral analysis of each sub-image, and the calculation results are shown in Fig. 4 and Table 3.

The calculated wavelength was applied as the main wave wavelength of the sub-images, and then the depths at the center of the sub-images in the reference bathymetry were searched. Wave period could be obtained by substituting the wavelength and water depth into Eq. (4). In shallow water areas, the wave period typically does not vary distinctly, so the average wave period based on the four sub-images (T=13.43 s) was adopted as the wave period in the whole detection area. According to the linear dispersion property, $L < \frac{gT^2}{2\pi}$, the maximum wavelength is 281 m for T=13.43 s.

(2) Wavelength calculation

The wave tracking algorithm is as follows: first, a starting point is selected in the image far from the shoreline, and this starting point is applied as the center of the Fourier transform operation (the size of the Fourier transform box is generally an integer power of 2, such as 256 or 512) to determine the wavelength and wave direction. Then, n times the wavelength is propagated along the wave direction to the next tracking point, and the above process is repeated until the wave reaches the shore. During wave propagation, to avoid overlap of the different wave systems, successive wave directions should be constrained to deviate by no more than 15° from the next wave direction over the previous wave direction. The wave tracking process is shown in Fig. 2.

In this experiment, the Fourier transform box size was set to 256×256 pixels (approximately 2 km×2 km) and the number of waves tracked was set to 50, with the propagation distance asset to the wavelength value. Since 50 wave rays overlapped in the graph, only 20 wave rays were selected for display in Fig. 5. The maximum value of the traced wavelength reached 1 021 m (certain image areas contained noise, which could cause an excessive calculated wavelength value), and the minimum value was 63 m. Any wavelength values less than cut-off wavelength were excluded when calculating water depth.

3.3 *Topography detection results*

The bathymetry value can be calculated by substituting the inverse wavelength and wave period into Eq. (4), but not every bathymetry value is accurate. In this paper, the bathymetry points with large errors were eliminated, and then kriging interpolation and two-dimensional low-pass filtering were performed to obtain the detection topography map. Figure 6 shows the results for five parameter images, among which α has the smallest error with an MRE of 12.56%, followed by VV polarization with an MRE of 12.87%, and HV polarization has the worst accuracy with an MRE of 14.11%.

The parameter α had the highest detection accuracy in the four study areas, and the corresponding detection topography is shown in Fig. 7. The depths in study area A ranged from 10 m to 30 m, with a general increasing trend of the depth along the direction of increasing latitude and longitude, values under less notable topography changes. The depth in study area B ranged from 20 m to 80 m. The topographic gradient in the blue and green

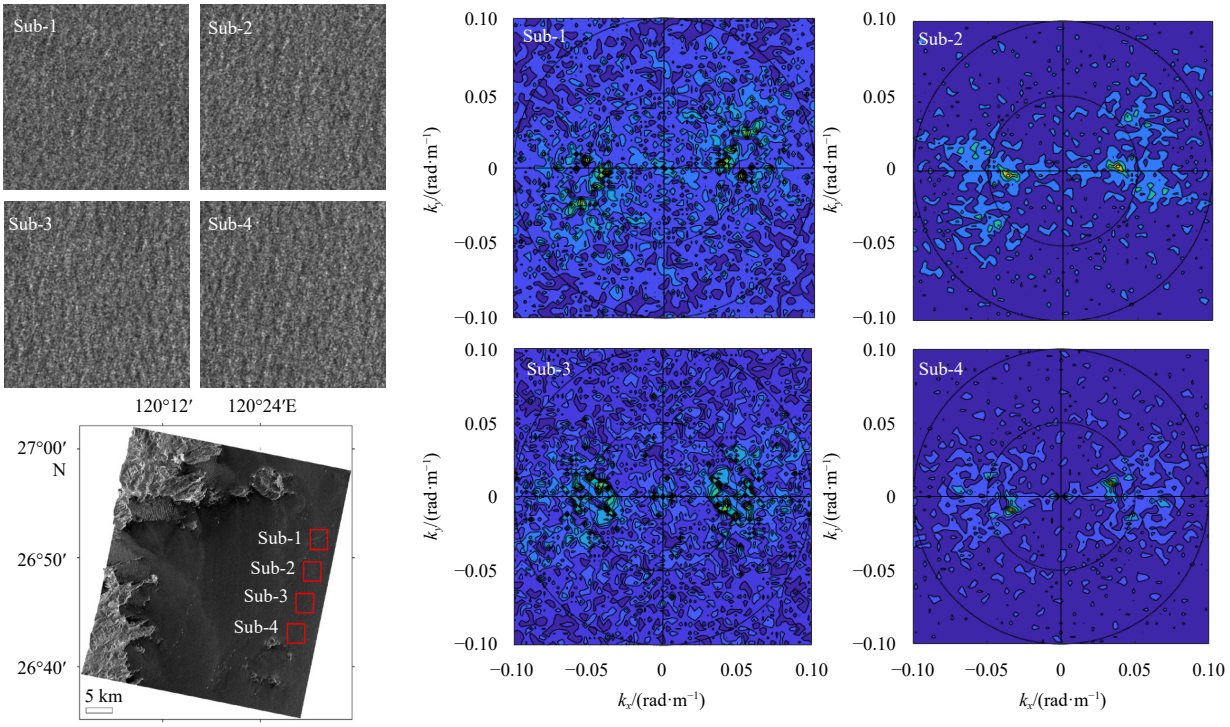

Fig. 4. Schematic diagram of the wave estimation of HH polarized image in study area C. Sub-1, Sub-2, Sub-3 and Sub-4 are 256×256 pixel areas, with the four sub images on the top left and the spectrograms of the four sub images on the right.

Table 3. Wave parameters of the sample areas

Sub-image	Wavelength/m	Reference depth/m	Wave period/s
Sub-1	157.07	15.40	13.55
Sub-2	170.08	18.58	13.53
Sub-3	168.34	19.80	13.10
Sub-4	179.62	21.06	13.55

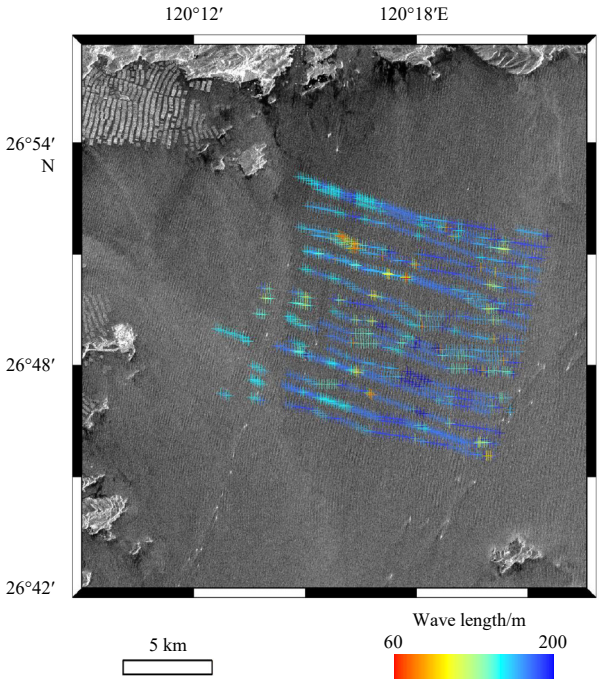

Fig. 5. Schematic diagram of the wave tracking process in the HH-polarized image of the study area C, only 20 wave rays are shown for clarity.

parts of Fig. 7b is low, with water depth values of approximately 30 m and 65 m, respectively. At the junction of these two areas, the topography changed dramatically, with the water depth values rapidly declining from 40 m to 60 m. Study area C exhibited a depth range from 9 m to 17 m with little variation in the water depth. The bathymetry in study area D ranged from 4 m to 20 m, with the topography decreasing slowly along a southwesterly direction. The direction of detected topography variation corresponded to the direction of the actual topographic variation in all four study areas, with a gradual increase in the bathymetry values from nearshore to offshore.

4 Discussion

Figure 8 represents the error variation in the different parameters. There is inconspicuous variation in MRE among the different parameters, but with larger differences in MAE. Although the MRE does not reflect the variation between the different parameters in the same study area, this index can effectively represent the detection error between the different study areas. Therefore, the MAE is mainly considered in the error analysis of the different parameters within the same study area, while the MRE is mainly applied in the error analysis of the different study areas.

4.1 *Analysis of the detection capabilities for different parameters*

α had the best detection with MAEs of 2.8 m, 5.2 m, 1.66 m and 1.64 m, and MRE of 14.52%, 10.30%, 12.56% and 12.90%, respectively, in the four study areas. The detection errors of co-polarized HH and VV were not distinctly different but were worse than that of α. The detection errors of cross-polarized HV and VH were unsatisfactory.

Generally, the sea surface rarely occurs multiple scatters in low and medium sea conditions, so the sea surface backscattering signals received by cross-polarization are weak, which is not

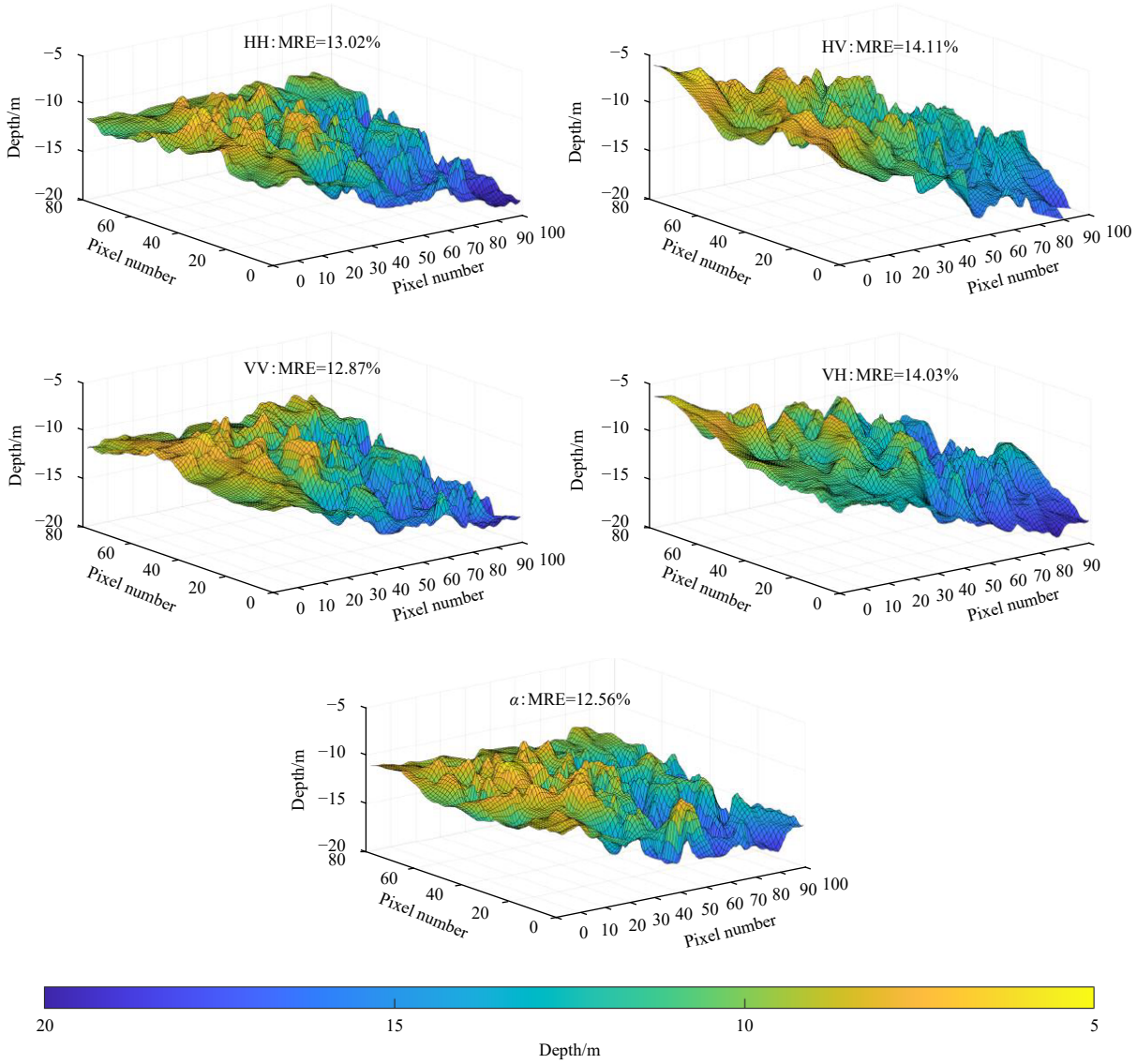

Fig. 6. Detection topography maps of seven parameters in study area C.

conducive to the extraction of wave wavelengths (Jackson and Apel, 2004). This phenomenon leads to the unsatisfactory effect of cross-polarized images in shallow sea topography detection. Conversely, co-polarization can obtain stronger backscattered signals, which is also more advantageous in topography detection. The backscattered signals of VV polarization are stronger than those of HH polarization (Romeiser and Alpers, 1997). However, given the results in this paper, there is no significant difference between HH and VV polarization for shallow sea topography detection.

Polarization features can effectively distinguish scattering differences between specific sea targets (ships, oil spills and sea ice) or medium-scale dynamic phenomena (internal waves) and the sea surface background (Liu et al., 2019; Shu et al., 2020; Zhang et al., 2015, 2020). Shallow sea topography detection mainly relies on the wave streaks on SAR images. In contrast to other sea targets and sea surface backgrounds with large scattering differences, the difference in wave information between different polarization features is not obvious, but they still provide a certain ability to recognize waves. Sea surface scattering has complex mechanisms. Under moderate incidence angle and moderate wind speed conditions, sea surface scattering is dominated by Bragg surface scattering, while secondary scattering, bulk scattering and spiral scattering mechanisms also exist.

Co-polarized or cross-polarized SAR data generally represents backscattered intensity and requires complex modulation functions to obtain the wave spectrum. Fully polarimetric data can provide more relevant electromagnetic scattering information, such as orientation angle and polarization scattering angle (α). These parameters have been proved that are more sensitive to the sea surface slope in a specific direction, which can effectively and directly retrieve wave spectrum. To some extent, the parameters also can improve the precision of shallow sea topography detection based on swell patterns.

The polarization scattering parameter α is the main parameter for identifying sea surface scattering, and it is sensitive to both the magnitude and direction of the wave slope in the range direction. Thus, it can preferably represent the variation in wave texture. Waves propagated almost along the range direction in the four study areas, so α had an ideal performance compared to quad-polarized images in shallow sea topography detection.

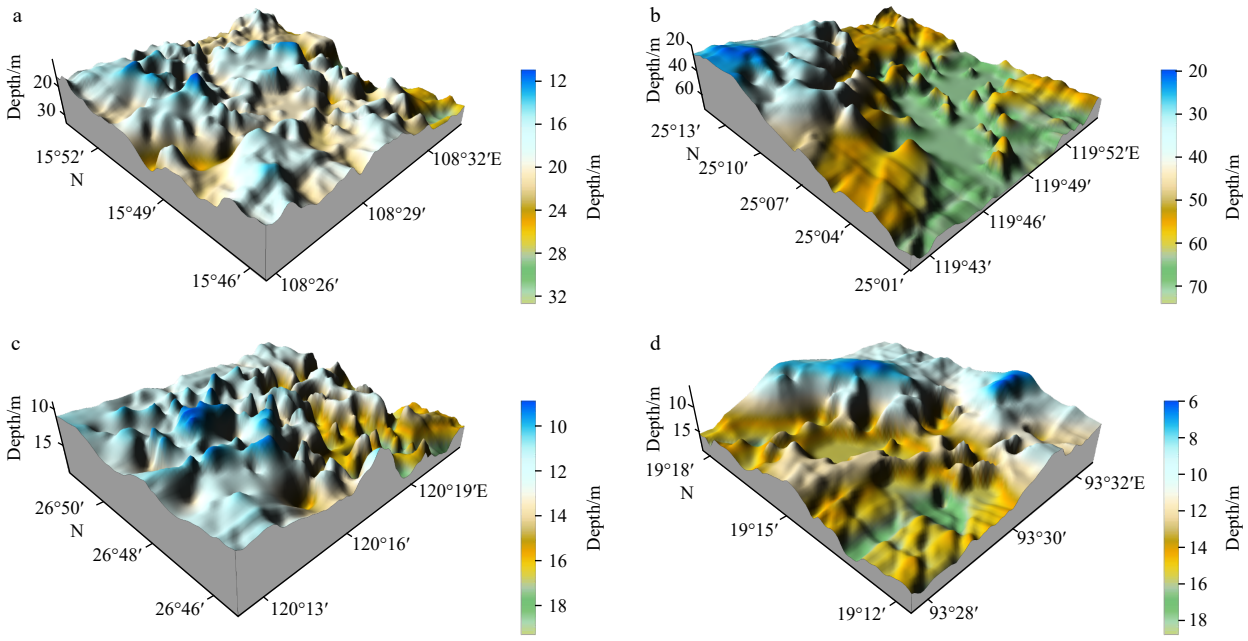

Fig. 7. Detection topography maps of the four study areas. a. The eastern sea of Hoi An, Vietnam; b. the southern sea of Pingtan County, Fujian Province, China; c. the eastern sea of Xiapu County, Fujian Province, China; d. the western sea of Rakhine State, Myanmar.

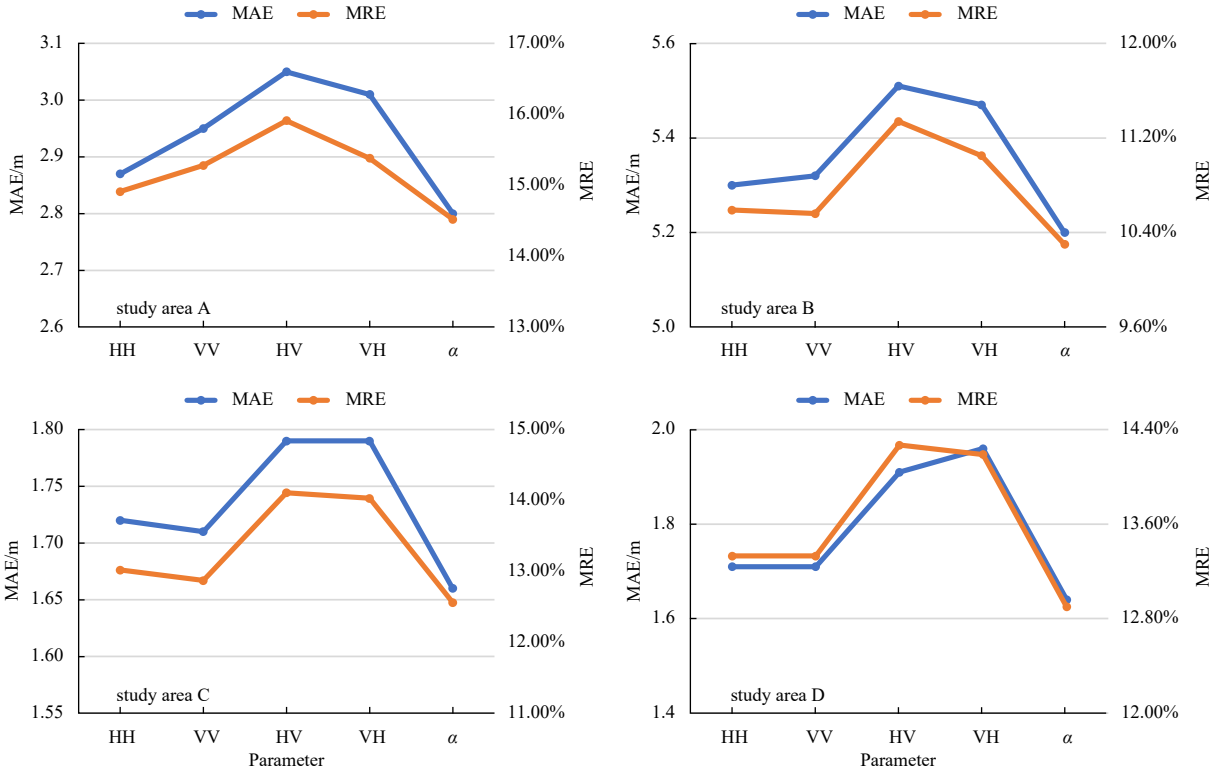

Fig. 8. Plot of the error variation in the different parameters. Polarization does not have an apparent influence on the first shallow sea topography detection method based on SAR imagery, but the approach used in this paper relies on the imaging of surface waves, so the detection capability of different polarization images differs greatly, which is mainly reflected between the co-polarization and cross-polarization. MAE: mean absolute error; MRE: mean relative error.

4.2 *Analysis of the detection capabilities in the area with different topographies*

As shown in the reference topography in Fig. 9. The topography is complex, with an irregular isobath distribution and local "peak" in study area A. The histogram in Fig. 9a shows the detection accuracy at different depths, and 20–25 m had the highest accuracy with MRE of 12.04%. The worst detection was at 10–15 m, where the area existed raised "peak" topography, as shown by the red arrows in Fig. 9a. In study area B, the detection accuracy is higher in 30–60 m, and the map represents that the topography

varies uniformly and has regular isobaths in the area. Figure 9 displays that the topographic gradient in the 50–60 m is significantly greater than the 30–50 m. However, the accuracy of topography detection was reversed. We hypothesized that a smaller

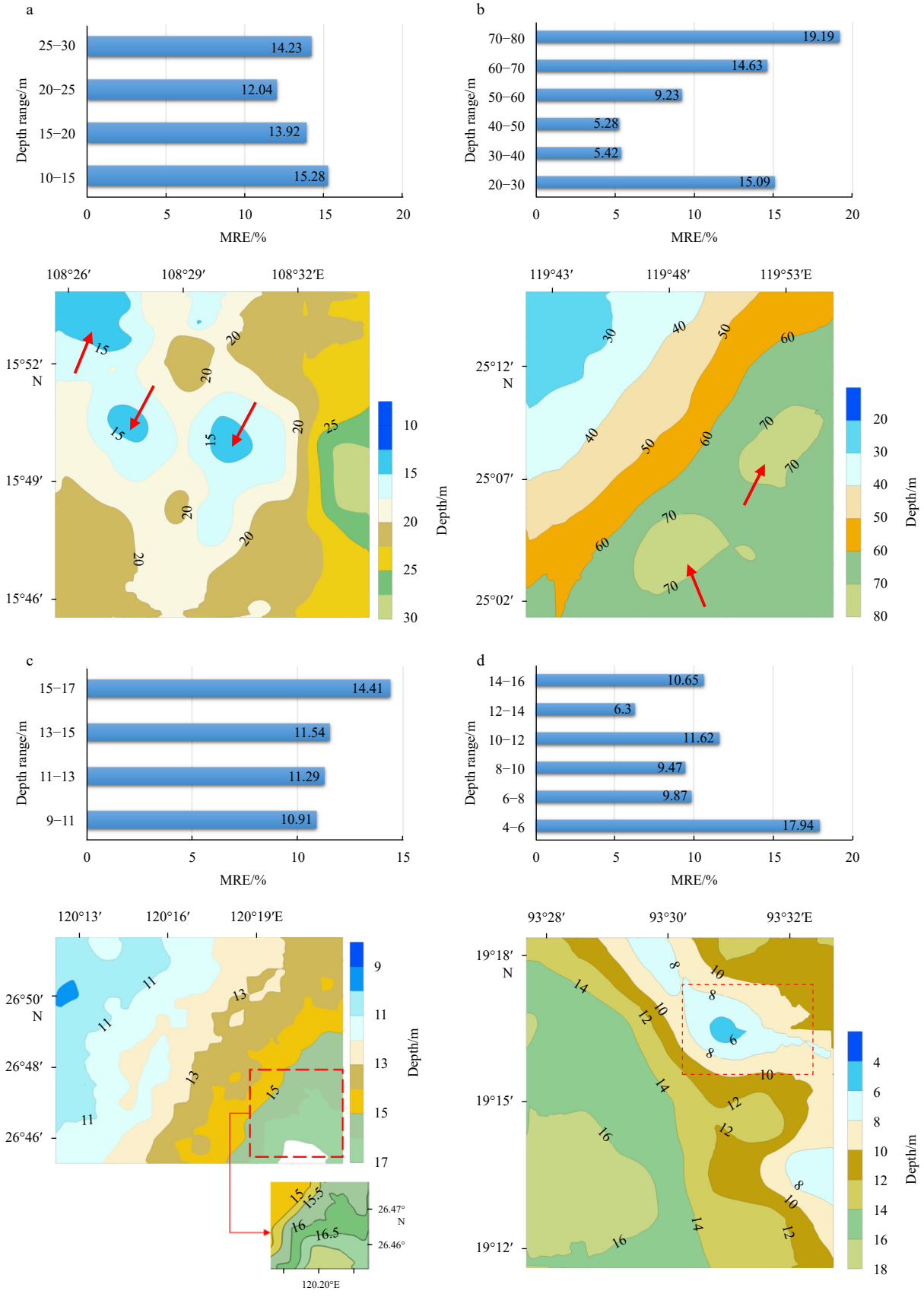

Fig. 9. Reference topography map and error histograms corresponding to different depths.

topography gradient may benefit topographic detection. There were two "peaks" at depths of 60–80 m, so its detection accuracy was low. The topography of study area C changed slowly, and the isobath distribution was irregular. The area with depths of 9–15 m had a similar detection accuracy. The detection accuracy in 15–17 m was worst and the MRE was 14.41%. Figure 6 shows that the waves are propagating in a north-westerly direction and that the topography change direction in 15–17 m is almost perpendicular to the direction of wave propagation (red dashed box in Fig. 9c), which may be the reason for the low detection accuracy in this area. In Study Area D, the highest detection accuracy was in the 11–13 m, with an MRE of 7.19%, and 5–7 m and 7–9 m were a "peak" terrain, both of which had a higher detection error of 13.35% and 16.22%, respectively.

This detection model has apparent discrepancies in response to different topographies. The scale of topography gradient, the relationship between the direction of topography gradient and swell propagation and the distribution of isobaths all influence the topography detection. In the four study areas, study area B had the highest detection accuracy, followed by study areas D and C, and the worst detection was in study area A. Combined with the above analysis, we conclude that the regular isobath is conducive to the propagation of waves, which also occurs in topography detection because the direction of wave propagation and isobath have a gradual vertical trend. In addition, the topography detection model performs well when the direction of topography gradient and wave propagation are close or the topography changes slowly. However, for the "peak" terrain, the detection effect is unsatisfactory.

5 Conclusions

Based on swell patterns, this paper proposed a fully polarimetric SAR shallow-sea topography detection model and preliminarily analyzed the feasibility of fully polarimetric SAR data in shallow-sea topography detection. Four offshore areas suitable for topography detection were selected, and the four corresponding scenes of fully polarimetric Gaofen-3 SAR images were collected for experiments. The topography detection errors for the four study areas were 14.52%, 10.30%, 12.56% and 12.90%, respectively.

The results demonstrate the responsiveness of the SAR shallow sea topography detection model based on swell patterns. In coastal waters, swell propagation generally occurs perpendicular to the direction of the isobath distribution. The swell calculation accuracy determines the topography detection accuracy. The model proposed in this paper is suitable for topography with small gradient and regular isobaths.

For each study area, five parameters were adopted to detect the topography, including quad-polarimetric images and α images. The results demonstrated that α had a better performance in shallow topography detection. Compared with co-polarization or cross-polarization data, the error based on fully polarimetric SAR improved. Fully polarimetric SAR provides extensive data on ocean parameters, so they can be used to complement the results of single-polarized SAR data in topography detection. The launch of the Gaofen-3 satellite provided us with abundant fully polarimetric SAR data, and only α was applied in this paper. In the future, more alternative polarization decomposition techniques should be considered in shallow sea topography detection.

Acknowledgements

We gratefully acknowledge the National Satellite Ocean Application Service for providing the GF-3 SAR productions. Furthermore, we gratefully acknowledge Satellite Geodesy and British Oceanographic Data Centre for providing SRTM 15+ and GEBCO depth data of study area. Finally, we sincerely thank the two anonymous reviewers for their comments and the editors for their work.

References

Alpers W, Hennings I. 1984. A theory of the imaging mechanism of underwater bottom topography by real and synthetic aperture radar. Journal of Geophysical Research, 89(C6): 10529–10546, doi: 10.1029/JC089iC06p10529

Beal R C, Tilley D G, Monaldo F M. 1983. Large-and small-scale spatial evolution of digitally processed ocean wave spectra from SEASAT synthetic aperture radar. Journal of Geophysical Research, 88(C3): 1761–1778, doi: 10.1029/JC088iC03p01761

Bian Xiaolin, Shao Yun, Tian Wei, et al. 2016. Estimation of shallow water depth using HJ-1C S-band SAR data. The Journal of Navigation, 69(1): 113–126, doi: 10.1017/S0373463315000454

Bian Xiaolin, Shao Yun, Wang Shiang, et al. 2018. Shallow water depth retrieval from multitemporal sentinel-1 SAR data. IEEE Journal of Selected Topics in Applied Earth Observations and Remote Sensing, 11(9): 2991–3000, doi: 10.1109/JSTARS.2018.2851845

Bian Xiaolin, Shao Yun, Zhang Chunyan, et al. 2020. The feasibility of assessing swell-based bathymetry using SAR imagery from orbiting satellites. ISPRS Journal of Photogrammetry and Remote Sensing, 168: 124–130, doi: 10.1016/j.isprsjprs.2020.08.006

Boccia V, Renga A, Moccia A, et al. 2015a. Tracking of coastal swell fields in SAR images for sea depth retrieval: application to ALOS L-band data. IEEE Journal of Selected Topics in Applied Earth Observations and Remote Sensing, 8(7): 3532–3540, doi: 10.1109/JSTARS.2015.2418273

Boccia V, Renga A, Rufino G, et al. 2014. L-band SAR image processing for the determination of coastal bathymetry based on swell analysis. In: Proceedings of 2014 IEEE Geoscience and Remote Sensing Symposium. Quebec City, Canada: IEEE, 5144–5147, doi: 10.1109/IGARSS.2014.6947656

Boccia V, Renga A, Rufino G, et al. 2015b. Linear dispersion relation and depth sensitivity to swell parameters: application to synthetic aperture radar imaging and bathymetry. The Scientific World Journal, 2015: 374579

Bruck Sr M, Lehner S. 2013. Coastal wave field extraction using TerraSAR-X data. Journal of Applied Remote Sensing, 7(1): 073694, doi: 10.1117/1.JRS.7.073694

Brusch S, Held P, Lehner S, et al. 2011. Underwater bottom topography in coastal areas from TerraSAR-X data. International Journal of Remote Sensing, 32(16): 4527–4543, doi: 10.1080/01431161.2010.489063

Calkoen C J, Hesselmans G H F M, Wensink G J, et al. 2001. The Bathymetry Assessment System: efficient depth mapping in shallow seas using radar images. International Journal of Remote Sensing, 22(15): 2973–2998, doi: 10.1080/01431160116928

Cloude S R, Pottier E. 1997. An entropy based classification scheme for land applications of polarimetric SAR. IEEE Transactions on Geoscience and Remote Sensing, 35(1): 68–78, doi: 10.1109/36.551935

Collard F, Ardhuin F, Chapron B. 2005. Extraction of coastal ocean wave fields from SAR images. IEEE Journal of Oceanic Engineering, 30(3): 526–533, doi: 10.1109/JOE.2005.857503

Fan Kaiguo, Huang Weigen, He Mingxia, et al. 2008. Depth inversion in coastal water based on SAR image of waves. Chinese Journal of Oceanology and Limnology, 26(4): 434–439, doi: 10.1007/s00343-008-0434-4

Hasselmann K, Raney R K, Plant W J, et al. 1985. Theory of synthetic aperture radar ocean imaging: A MARSEN view. Journal of Geophysical Research, 90(C3): 4659–4686, doi: 10.1029/JC090iC03p04659

Huang Longyu, Yang Jungang, Meng Junmin, et al. 2021. Underwater topography detection and analysis of the Qilianyu Islands in the South China Sea based on GF-3 sar images. Remote Sensing, 13(1): 76, doi: 10.3390/rs13010076

Jackson C R, Apel J R. 2004. Synthetic aperture radar marine user's manual. Washington: U. S. Department of Commerce

Kirby J T, Dalrymple K. 1986. An approximate model for nonlinear dispersion in monochromatic wave propagation models. Coastal Engineering, 9(6): 545–561, doi: 10.1016/0378-3839(86)90003-7

Li Xiaoming, Lehner S, Rosenthal W. 2010a. Investigation of ocean surface wave refraction using TerraSAR-X Data. IEEE Transactions on Geoscience and Remote Sensing, 48(2): 830–840, doi: 10.1109/TGRS.2009.2033177

Li Xiaofeng, Li Chunyan, Xu Qing, et al. 2009. Sea surface manifestation of along-tidal-channel underwater ridges imaged by SAR. IEEE Transactions on Geoscience and Remote Sensing, 47(8): 2467–2477, doi: 10.1109/TGRS.2009.2014154

Li Xiaofeng, Yang Xiaofeng, Zheng Quanan, et al. 2010b. Deep-water bathymetric features imaged by spaceborne SAR in the Gulf Stream region. Geophysical Research Letters, 37(19): L19603, doi: 10.1029/2010GL044406

Liu Genwang, Zhang Xi, Meng Junmin. 2019. A small ship target detection method based on polarimetric SAR. Remote Sensing, 11(24): 2938, doi: 10.3390/rs11242938

Mishra M K, Ganguly D, Chauhan P, et al. 2014. Estimation of coastal bathymetry using RISAT-1 C-band microwave SAR data. IEEE Geoscience and Remote Sensing Letters, 11(3): 671–675, doi: 10.1109/LGRS.2013.2274475

Misra A, Ramakrishnan B, Muslim A M. 2022. Synergistic utilization of optical and microwave satellite data for coastal bathymetry estimation. Geocarto International, 37(8): 2323–2345, doi: 10.1080/10106049.2020.1829100

Pereira P, Baptista P, Cunha T, et al. 2019. Estimation of the nearshore bathymetry from high temporal resolution Sentinel-1A C-band SAR data—A case study. Remote Sensing of Environment, 223: 166–178, doi: 10.1016/j.rse.2019.01.003

Pleskachevsky A, Lehner S, Heege T, et al. 2011. Synergy and fusion of optical and synthetic aperture radar satellite data for underwater topography estimation in coastal areas. Ocean Dynamics, 61(12): 2099–2120, doi: 10.1007/s10236-011-0460-1

Qi Yali. 2009. A relevance feedback retrieval method based on Tamura texture. In: Proceedings of the 2009 Second International Symposium on Knowledge Acquisition and Modeling. Wuhan: IEEE, 174–177

Romeiser R, Alpers W. 1997. An improved composite surface model for the radar backscattering cross section of the ocean surface: 2. Model response to surface roughness variations and the radar imaging of underwater bottom topography. Journal of Geophysical Research, 102(C11): 25251–25267, doi: 10.1029/97JC00191

Santos D, Abreu T, Silva P A, et al. 2020. Estimation of coastal bathymetry using wavelets. Journal of Marine Science and Engineering, 8(10): 772, doi: 10.3390/jmse8100772

Santos D, Fernández-Fernández S, Abreu T, et al. 2022. Retrieval of nearshore bathymetry from Sentinel-1 SAR data in high energetic wave coasts: the Portuguese case study. Remote Sensing Applications: Society and Environment, 25: 100674, doi: 10.1016/j.rsase.2021.100674

Schuler D L, Lee J S, Kasilingam D, et al. 2004. Measurement of ocean surface slopes and wave spectra using polarimetric SAR image data. Remote Sensing of Environment, 91(2): 198–211, doi: 10.1016/j.rse.2004.03.008

Schuler D L, Lee J S, Pottier E, et al. 2005. Comparison of polarimetric SAR techniques for the measurement of directional ocean wave spectra. In: Proceedings of 2005 IEEE International Geoscience and Remote Sensing Symposium. Seoul: IEEE, 4

Shen Simin, Zhu Shouxian, Kang Yanyan, et al. 2019. Simulation analysis for remote sensing inversion of wavelength and water depth by the Fast Fourier Transform method. Journal of East China Normal University (Natural Science), 2019(2): 189–194, 208

Shu Sijing, Meng Junmin, Zhang Xi, et al. 2020. Experimental study of C-band microwave scattering characteristics during the emulsification process of oil spills. Acta Oceanologica Sinica, 39(7): 135–145, doi: 10.1007/s13131-020-1612-4

Tozer B, Sandwell D T, Smith W H F, et al. 2019. Global bathymetry and topography at 15 Arc Sec: SRTM15+. Earth and Space Science, 6(10): 1847–1864, doi: 10.1029/2019EA000658

Weatherall P, Tozer B, Arndt J E, et al. 2021. The GEBCO_2021 Grid - a continuous terrain model of the global oceans and land. Liverpool: NERC EDS British Oceanographic Data Centre NOC

Zhang Xi, Dierking W, Zhang Jie, et al. 2015. Retrieval of the thickness of undeformed sea ice from C-band compact polarimetric SAR images. The Cryosphere Discussions, 9(5): 5445–5483

Zhang Hao, Meng Junmin, Sun Lina, et al. 2020. Performance analysis of internal solitary wave detection and identification based on compact polarimetric SAR. IEEE Access, 8: 172839–172847, doi: 10.1109/ACCESS.2020.3025946

Zhao Wei, Zhou Guoqing, Yue Tao, et al. 2013. Retrieval of ocean wavelength and wave direction from sar image based on radon transform. In: Proceedings of 2013 IEEE International Geoscience and Remote Sensing Symposium. Melbourne: IEEE, 1513–1516

Zheng Quanan, Holt B, Li Xiaofeng, et al. 2012. Deep-water seamount wakes on SEASAT SAR image in the Gulf Stream region. Geophysical Research Letters, 39(16): L16604, doi: 10.1029/2012GL052661

Appendix A: $H/A/\alpha$ decomposition

$H/A/\alpha$ decomposition was proposed by Cloude and Pottier (1997). Entropy, anisotropy and alpha can be extracted from fully polarimetric SAR data using $H/A/\alpha$ decomposition. The main idea of the method is to decompose the coherence matrix $\boldsymbol{T}_3$ into three independent scattering mechanisms, and $\boldsymbol{T}_3$ can be expressed as

$$\boldsymbol{T}_3 = [U_3] \cdot \begin{bmatrix} \lambda_1 & 0 & 0 \\ 0 & \lambda_2 & 0 \\ 0 & 0 & \lambda_3 \end{bmatrix} \cdot [U_3]^{*\mathrm{T}}, \tag{A1}$$

where

$$[U_3] = \mathrm{e}^{j\varphi} \begin{bmatrix} \cos\alpha_1 & \cos\alpha_2 \mathrm{e}^{j\varphi_2} & \cos\alpha_3 \mathrm{e}^{j\varphi_3} \\ \sin\alpha_1 \cos\beta_1 \mathrm{e}^{j\delta_1} & \sin\alpha_2 \cos\beta_2 \mathrm{e}^{j\delta_2} & \sin\alpha_3 \cos\beta_3 \mathrm{e}^{j\delta_3} \\ \sin\alpha_1 \sin\beta_1 \mathrm{e}^{j\gamma_1} & \sin\alpha_2 \sin\beta_2 \mathrm{e}^{j\gamma_2} & \sin\alpha_3 \sin\beta_3 \mathrm{e}^{j\gamma_3} \end{bmatrix}. \tag{A2}$$

Polarization scattering parameter α can be expressed as

$$\alpha = P_1\alpha_1 + P_2\alpha_2 + P_3\alpha_3, \tag{A3}$$

where

$$P_i = \frac{\lambda_i}{\sum_{j=1}^{j=3} \lambda_j}. \tag{A4}$$

Appendix B: Tamura texture features

Tamura texture features include six texture attributes, coarseness, contrast, orientation, linearity, regularity, and roughness, which not only express the texture information of images but also conform to the human visual perception of texture (Qi, 2009). Among them, coarseness and contrast are two important attributes.

(1) Coarseness

Coarseness is the most crucial feature in the texture, which can reflect the change degree of the gray value in the image pixels. Large coarseness indicates more textures in the image. It can be expressed as

$$\text{Coarseness} = \frac{1}{m \times n} \sum_{i=1}^{m} \sum_{j=1}^{n} S_{\text{best}}(i,j), \tag{B1}$$

where S_{best} is the best size among numerous field sizes when scanning every pixel of the entire image.

(2) Contrast

Contrast describes the brightness and reflects the statistical distribution of grayscale in the image. Assuming that μ_4 is the fourth-order moment of grayscale, σ^2 is the variance of image grayscale, and kurtosis $\sigma_4 = \frac{\mu_4}{\sigma^4}$, the mathematical expression of contrast is

$$\text{Contrast} = \frac{\sigma}{\sqrt[4]{\sigma_4}}. \tag{B2}$$